Alumina supported Cu nanoparticles derived from MOF crystallites for CO_2 hydrogenation

Adele T. Chalmers,[a] Zonggao Hu,[b] Nicholas F. Dummer, [b] Kieran J. Aggett, [b] David J. Morgan, [b] Michael Bowker, [b] Graham J. Hutchings [b] and Kara J. Stowers *[a]

A carbon economy hinges on sustainable treatment and usage of greenhouse gases. Copper-based catalysts are an efficient way to make use of one of the most common greenhouse gases, carbon dioxide. In this work, a metal–organic framework decomposition method was used to synthesize a copper catalyst that was active and reproducible for methanol production *via* CO_2 hydrogenation. The properties of the as-prepared and decomposed MOF catalysts were analyzed using a wide range of characterization techniques (*e.g.* SEM, TEM, ICP-MS, XRD, N_2 adsorption, TGA, XPS, H_2-TPR) to rationalize the layer-by-layer synthetic approach to form the subsequent supported Cu nanoparticles. The catalytic performance of the MOF derived catalyst was compared to that of a sol-immobilization prepared Cu/Al_2O_3 catalyst in a fixed-bed continuous flow reactor for CO_2 hydrogenation. The MOF derived catalyst formed from ten iterative layers performed similarly to the sol-immobilization prepared catalyst but displayed increased methanol productivity at all reaction temperatures tested. This work indicates that synthesis of copper-based catalysts through MOF-templating is a viable method that would be impactful for future incorporation of secondary metals such as Zn, Ce, and/or Al that are typical additions for catalytic conversion of CO_2 to methanol.

1. Introduction

The conversion of carbon dioxide to methanol is an impactful way that chemical processes could be closed loop and therefore contribute to a greener economy.[1] Additionally, the conversion of carbon dioxide to methanol using photo- or electro-chemically generated hydrogen would increase the impact toward mitigating the presence of this greenhouse gas.[2] Finally, the catalysts that are the most efficient and active for this transformation, copper-based materials, are also earth abundant and non-toxic.

Copper-based catalysts are well known for the transformation of carbon dioxide to methanol due to the favorable binding of carbon dioxide without splitting the C–O bond, H_2 adsorption and dissociation, as well as C–H bond formation.[3] Each of these steps are mediated by the copper surface. However, copper has also been known to aggregate, decreasing active site efficiency and thereby losing the reactivity of the catalyst over time.[4] Because of this, copper has been supported on a variety of materials such as aluminum- and zinc-based oxides.[5,6] Typically, γ-(Al_2O_3) is used as a support for such catalysts,[7] due to properties such as high thermal stability,[8] large surface area, and moderate pore volume. The material also has morphological properties that make it valuable, and is generally considered to have cubic defect spinel structure, which gives it partially uncoordinated oxygen and aluminum atoms that can participate in bonding.[9] More specifically, the oxides at the surface of the support are able to participate in Lewis acid/base interactions with the copper cations to create nucleation sites for metal–organic-framework (MOF) growth.[10]

The synthesis of supported copper catalysts can involve a number of methods, with traditional ones involving impregnation or sol–gel.[11] When size control is required, synthesis of nanoparticles prior to integration with the support is beneficial. While these methods generally produce active catalysts, there can be limitations due to the high sensitivity of the synthesis conditions, creating a lack of reproducibility and scalability. Thereby causing a lack of control over copper nanoparticle growth and a lack of control over catalyst metal weight loading and dispersion.[12] To address these challenges, a templated method can be employed that has a finely tuned ability to increase the copper

[a] *C100 Benson Building, Department of Chemistry and Biochemistry, Brigham Young University, Provo, UT 84602, USA. E-mail: kara.stowers@byu.edu*
[b] *Max Planck-Cardiff Centre on the fundamentals of heterogeneous catalysis FUNCAT, Cardiff Catalysis Institute, School of Chemistry, Cardiff University, Translational Research Hub, Cardiff, CF24 4HQ, UK*

loading on the support and provide control over nanoparticle size during synthesis at multiple stages.

One of the most flexible templates are MOFs, these modular materials include metals that are bound to carboxylate or amine-based ligands that make up a 2D or 3D network with periodic spacing between metals in the structure.[13] These can be made from a variety of ligands with metals. Many different MOFs are easily synthesized using a variety of methods and solvents.[14] Based on the periodic structure of the framework, the removal of the organic ligands can then produce small and evenly spaced nanoparticles when deposited on a support. Additionally, using MOF materials as a template for nanoparticles can assist in overcoming some of the challenging aspects: they are sometimes sensitive at high temperatures and water intolerant. As a template, thermal instability is a desirable feature. MOFs would be deposited as a thin film on a support, then thermally treated to obtain well distributed active nanoparticles.

Our hypothesis is that active supported nanoparticle catalysts can be created using a MOF thin film strategy that enables flexible control over composition while maintaining strong catalytic activity. The MOF template is expected to promote uniform nanoparticle size, dispersion, and surface properties by ensuring homogeneous composition prior to nanoparticle formation as based on previous results using a silicon support.[15] Additionally, heat transfer during matrix decomposition is improved due to the thin layer compared to other methods of bulk MOF decomposition.[16,17] In this work, Cu nanoparticles supported on high-surface-area γ-Al_2O_3 were derived from a metal–organic-framework applied to the γ-Al_2O_3 powder through a layer-by-layer (LBL) synthesis method. The amount of MOF is tunable based on cycles applied to the powder.[18] The MOF thin film catalyst precursor supported on the oxide and the derived active Cu-nanoparticle catalyst after MOF removal was characterized through TGA, N_2 adsorption isotherms, TEM, SEM, XRD, ICP-MS, H_2-TPR and/or XPS. The LBL10D catalyst derived from the decomposition of MOF supported on γ-alumina was compared to a catalyst prepared by a sol-immobilization technique for CO_2 hydrogenation. Results are described in terms of Cu oxidation state, nanoparticle size, and surface area.

2. Experimental

2.1 Materials

Boehmite was synthesized in-house at BYU using a method that uses aluminum isopropoxides and water to control pore size,[19–22] then calcinated at 600 °C for two hours to obtain γ-Al_2O_3. Copper(II) acetate monohydrate was obtained from spectrum. Copper(II) nitrate trihydrate (99%) was obtained from Honeywell Fluka. Trimesic acid (95%), poly(vinyl alcohol) (M_w 9000-10 000, 80% hydrolyzed), and sodium borohydride (99%) were obtained from Sigma Aldrich.

2.2 Catalyst preparation for LBL-MOF-alumina

In separate containers, 5 mM copper acetate and 3 mM trimesic acid solutions were prepared in ethanol and each was doped with 2% by volume of water to ensure MOF formation when applied to the support. The γ-Al_2O_3 was prepared by the preceding synthesis procedure[19–22] and placed into a beaker. The γ-alumina was treated with ligand or metal solutions with a ratio of 10 mL of solution for every 300 mg of γ-Al_2O_3 (support), this was stirred for five minutes then filtered with vacuum filtration using VWR 413 filter paper and washed three times with ethanol. Each round of metal solution, rinse, ligand solution, rinse is one cycle. The cycles were repeated 5, 10, or 15 times as indicated. As the number of cycles increases the color of the γ-alumina gradually shifts from white to a teal blue color. After the desired number of cycles were completed, the samples were dried for 24 hours at 150 °C under ambient conditions. After drying, samples were stored under vacuum. The resultant materials are referred hereafter as LBL*x* where LBL stands for the layer-by-layer approach, *x* = number of cycles applied for the deposition of MOF crystallites grown directly onto the γ-alumina support.

The samples were decomposed in two stages. First, the sample is heated under static air to 350 °C with a 3 °C min^{-1} ramp rate. The sample was held at this temperature for 2 hours then allowed to cool naturally. After the first decomposition, the sample was loaded into a thin-walled flow-reactor-tube and loaded into a flow reactor. The sample was flushed with 100% H_2 for 1 hour with a flow rate of 10 ml min^{-1}. The sample was then heated to 250 °C with a 3 °C min^{-1} ramp rate and held for 2 hours. The sample was allowed to cool naturally. After decomposing, the samples were stored under vacuum, and denoted as LBL*x*D, where LBL stands for the layer by layer approach, *x* = number of cycles applied for the deposition of MOF crystallites grown directly onto the γ-alumina support, and D indicates the sample has been decomposed.

Preparation of bulk HKUST-1 is described in the SI.

2.3 Synthesis of γ-Al_2O_3 supported Cu catalysts by sol-immobilization

For the synthesis, 200 mL of aqueous solution of poly(vinylpyrrolidone) (PVA, M_w 9000-10 000, 80% hydrolyzed, PVA : Cu mass ratio = 1 : 1) was mixed with 200 mL of aqueous solution of $Cu(NO_3)_2 \cdot 3H_2O$ (0.76 g) in a 1 L beaker. A freshly prepared 100 mL aqueous solution of $NaBH_4$ (Na : Cu molar ratio = 5 : 1) in an ice bath was then added rapidly to the mixed solution under constant stirring at room temperature. After 30 minutes, 200 mL of aqueous suspension of γ-Al_2O_3 (1.8 g) was added under constant stirring. After 2 hours, the solid product was filtered and washed with 5 L deionized water and dried in an oven at 110 °C for 16 hours. The dried product was calcined at 350 °C for 4 hours under flowing air and reduced at 250 °C for 4 hours under flowing 5% H_2/Ar

gas, and the final sample was referred to as 10% Cu/γ-Al_2O_3.

2.4 Characterization

X-ray diffraction (XRD) measurements were performed in a Bruker D8 Venture. Each sample was first ground to a fine powder as needed. Then they were loaded into a 0.0122″ ID polyimide capillary (Cole-Parmer). Data collection was performed at room temperature using a 0.2 mm collimator, Cu X-ray source, and phi 360 scans. The detector distance was set to 100 nm. The omega and kappa angles were set to 104° and 0° respectively. Scans had a 600 sec/scan rate and were taken in dynamic mode. Duplicate scans were taken at each 2θ.

X-ray photoelectron spectroscopy (XPS) analysis was performed using a Kratos Axis Ultra DLD system utilising a monochromatic Al Ka X-ray source operating at 120 W (10 mA × 12 kV). Data was collected with pass energies of 160 eV for survey spectra, and 40 eV for high-resolution scans with step sizes of 1 eV and 0.1 eV respectively. The system was operated in the Hybrid mode, which uses a combination of magnetic immersion and electrostatic lenses and acquired over a rectangular area approximately 300 × 700 μm^2. A magnetically confined low energy electron charge compensation system was used to minimize charging of the sample surface, and all spectra were taken with a 90° take off angle. A base pressure of *ca.* 2 × 10^{-9} Torr was maintained during collection of the spectra. Data was analysed using CasaXPS (v2.3.27 PR3.9)[23] after subtraction of a Shirley background and using modified Wagner sensitivity factors as supplied by the manufacturer. Peak fits were performed using the LA line-shape in CasaXPS which forms a pseudo-Voigt function. All data is calibrated to the C–C C(1s) peak of adventitious carbon, taken to be 284.8 eV, this results in a binding energy uncertainty of ±0.25 eV.[24]

For inductively coupled plasma-mass spectrometry (ICP-MS) measurements, LBL*x* samples were digested in concentrated nitric acid (68–70 w/w%) (Fisher Chemical certified ACS) for 1 hour then the samples were diluted to contain 2% (w/w%) nitric acid. The samples were analyzed on an Agilent 7800 ICP-MS.

Surface area and pore volumes were acquired using a Micromeritics TriStar II surface area and porosity instrument. Samples were degassed in N_2 for 16 hours and then analyzed by multipoint BET analysis under N_2 at 77 K.

A Micrometrics 3Flex instrument was used for temperature program reduction (TPR) analysis. An onboard thermal conductivity detector was used to collect the data. A dry ice/isopropanol bath was used to collect any gaseous water produced. For the analysis, an H_2-Ar mixture obtained from Airgas (10.14 ± 2% mol H_2, lot 18-400657954-1), was flowed over the catalyst with a 2.231 mmol min^{-1} flow rate. The temperature range was room temperature to 800 °C with a 10 °C min^{-1} ramp rate.

Dynamic thermogravimetric (TGA) analysis was performed on a Netzsch STA 449 F5 Jupiter. The samples were heated in an open 0.3 ml Al_2O_3 crucible under N_2 from 30–1000 °C. Analysis of the samples was done with a 5 °C min^{-1} heating rate, 15 points per °C acquisition rate and 75 points per min acquisition rate.

Scanning electron microscopy (SEM) images were collected using a Verios G4 UC instrument in immersion mode. Images were taken using a 10 kV and 50 pA beam. Scanning transmission electron microscopy images (STEM), EDX linescans, and selected-area electron diffraction (SAED) patterns were collected using a Tecnai F20 instrument with gun lens 6, spot size 9, and CL (cathodoluminescence) 52.

2.5 Catalyst testing

Catalytic activity for the CO_2 hydrogenation reaction was assessed using a 16-bed high throughput reactor, designed, and manufactured by Integrated Lab Solutions GmbH (ILS). The reactor was of a fixed bed, continuous flow design with all beds operating under the same reaction conditions. A combination of Siemens Win CC software and Integrated Workflow manager, based on LabView software, was used to operate and automate the reactor. A capillary distribution system combined with Equilibar back pressure regulators were used to control the gas feed and pressure in each bed. The reactor was divided into four heating blocks, with four beds in each block. A thermocouple was positioned in each block to monitor the reaction temperature.

Pelleted catalysts (0.1 g, 425–600 μm), mixed with F80 silicon carbide (mean particle size 190 μm) were centered in the isothermal zone of a stainless steel tube (I.D. 4.00 nm), and supported on a bed of F24 silicon carbide (particle size 750 μm), to limit mass transfer. The catalysts were reduced *in situ* using a flow of 5% H_2/N_2 gas (40 ml min^{-1} 250 °C, 1 hour, 5 °C min^{-1}) prior to testing and subsequently cooled to 125 °C under flowing N_2. A reactant gas composition of 20% CO_2, 60% H_2, 5% Ar and 15% N_2 was used, with a flow rate of 30 ml min^{-1}. The system was then pressurized to 20 bar and left to stabilize for 4 hours before beginning the reaction. To limit product build-up in the downstream lines, a purge feed of N_2 (30 ml min^{-1}) was used and the downstream oven was set to 120 °C. The reaction was conducted at 230 °C, 250 °C and 270 °C. Reaction products were analyzed *via* online gas chromatography (Agilent 7890B system with two flame ionization detectors (FID) and a thermal conductivity detector TCD). Argon was used as an internal standard.

Four GC injections were taken at each temperature point, with a Vici stream selection valve used to switch between the beds. CO_2 conversion was calculated by comparing the moles of CO_2 in each bed to the moles of CO_2 in the calibration run at 125 °C. Methanol, carbon monoxide (CO), and dimethyl ether (DME) were the main products observed, with a minor contribution of methane. The carbon balance was calculated using the sum of

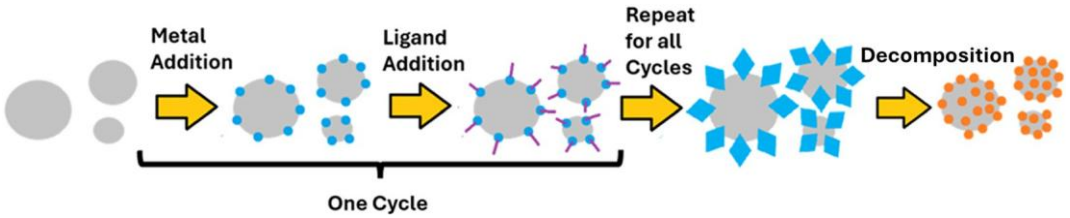

Fig. 1 Illustrated synthesis procedure of the MOF template for nanoparticles as grown on γ-Al_2O_3 (grey circles) support through an iterative layer-by-layer approach for Cu-MOF (blue diamonds) and following decomposition for the formation of Cu/Al_2O_3 (orange circles).

carbon containing products and reactants in the feed divided by the sum of carbon containing reactants in the calibration runs. Catalyst testing errors were calculated by running 12 commercial Cu/ZnO/Al_2O_3 (CZA) standards using the conditions stated. The error for CO_2 conversion was ± 1% and product selectivity was ± 2%.

3. Results and discussion

3.1 MOF-templated catalyst thin films supported on γ-Al_2O_3

In order to maximize Cu dispersion and control film thickness for efficient catalytic activity, we adopted a slow iterative layer-by-layer deposition of MOF onto high surface area γ-Al_2O_3.[18,25] While a quicker dip-coating of powders has been used in other methods,[26] our hypothesis was that a slower layered approach would ensure a uniform small layer distributed evenly on the surface.[27] The γ-Al_2O_3 used was selected based on high surface area and treatment conditions were selected as they have been reported to achieve the highest CO_2-to-methanol activity with Cu.[28] Using solutions of copper acetate in ethanol and trimesic acid in ethanol, the γ-Al_2O_3 support was iteratively treated with the metal solution, then ligand solution, with filtration, washing, and drying steps in between the applications of solutions (Fig. 1).

To correlate the growth and thickness of the MOF template on the γ-Al_2O_3 with numbers of application cycles and understand the impact on weight loading (wt%), the samples LBL*x* were synthesized, with *x* indicating the number of cycles applied. In this method, the metal salt initially adsorbs to the surface oxo- sites creating nucleation sites for the MOF to grow, while weakly adsorbed metals are removed in a wash step. The ligand solution that follows allows trimesic acid to attach to the bound Cu ions which then begins to build the MOF through interactions with the adsorbed metal ions in the previous step.

To determine the nominal loading of copper, samples were dissolved with nitric acid for elemental analysis with ICP-MS (Table 1). From the analysis, the amount of copper increased with an increasing number of cycles, from 5.0 wt% of Cu (LBL5) to 12.4 wt% (LBL15). This increase in Cu wt% is consistent with an increased growth of MOF thin film on the γ-Al_2O_3 support with increasing number of application cycles. Gratifyingly, the data indicates that the targeted wt% values of Cu were closely approximated by the number of application cycles up to 10 and then decreased only slightly thereafter.

The BET specific surface area falls from 265 $m^2\ g^{-1}$ of the bare γ-Al_2O_3 to 137 $m^2\ g^{-1}$ after five cycles (LBL5), then rebounds to 214 $m^2\ g^{-1}$ by LBL15 as shown in Table 1. Adsorption–desorption isotherms are illustrated in the SI (Fig. S1). The pore volumes decreased from 1.62 $cm^3\ g^{-1}$ for γ- Al_2O_3 to 1.16 $cm^3\ g^{-1}$ for LBL5 all the way to 0.88 $cm^3\ g^{-1}$ for LBL15. The specific surface area of the γ- Al_2O_3 support is relatively high at 265 $m^2\ g^{-1}$ but consistent with literature examples.[29,30] The MOF, while higher in specific surface area (369 $m^2\ g^{-1}$) than the γ-Al_2O_3 when activated, surprisingly decreased the overall surface area when on the surface of the γ-Al_2O_3.[31,32] However, as more MOF is added, the surface area increases to 205 and 214 $m^2\ g^{-1}$ for LBL10 and LBL15 respectively. This shift in surface area indicates that the MOF may block the pores of the γ-Al_2O_3, which then decreases the overall surface area. The observed increase in surface area with the increasing number of application cycles of MOF is consistent with an increased MOF layer thickness covering the surface of these materials despite further decreases in the pore volume.

The resultant powder samples were imaged with SEM to determine if the morphology resembles the non-supported MOF structure as well as to determine the MOF nanoparticle sizes; qualitative analysis of LBL5 indicated MOF crystallites

Table 1 Surface area properties of the alumina and MOF coated alumina powders, Cu loading, and weight loss through TGA analysis

Material	Specific surface area ($m^2\ g^{-1}$)	Pore volume ($cm^3\ g^{-1}$)	ICP wt% Cu	TGA wt% loss
Alumina	265	1.62	NA	0.80
LBL5	137	1.16	5.0 ± 0.6	10.4
LBL10	205	1.12	9.3 ± 0.7	14.4
LBL15	214	0.88	12.4 ± 0.4	19.0
Bulk HKUST-1[a]	369	0.20	NA[a]	32.1

[a] See SI for other details.

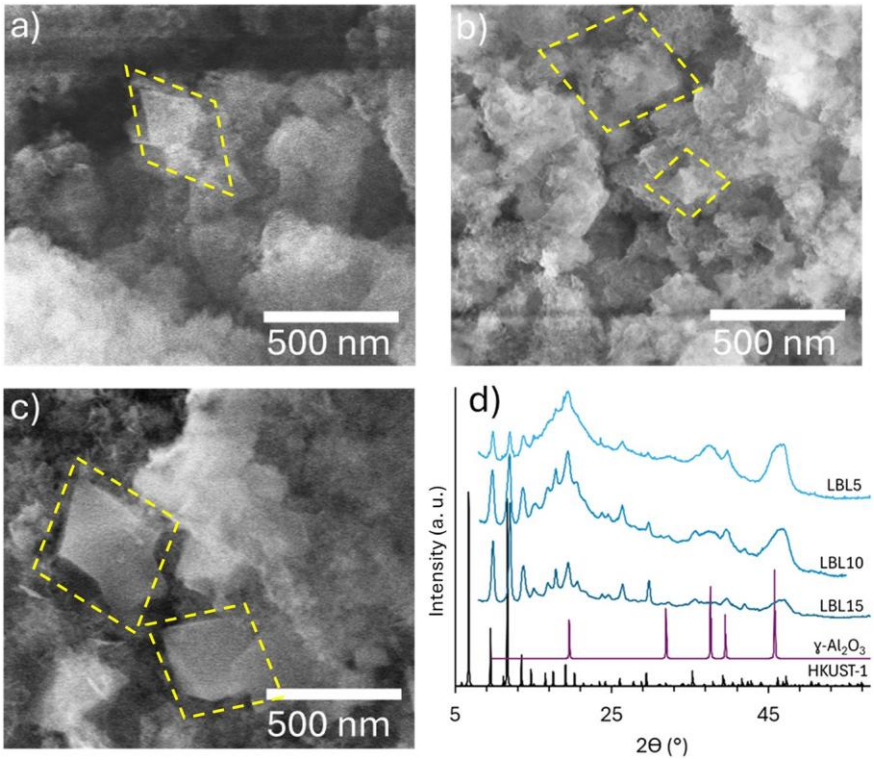

Fig. 2 SEM image of a) LBL5, b) LBL10, c) LBL15 with images of the powder and small octahedral crystallites surrounded by a dashed line, d) pXRD for LBL5, LBL10, and LBL15. Computationally modeled reference for HKUST-1 (PDF 00-065-1028) and γ-Al_2O_3 (PDF 00-029-0063) are also shown. Note: peaks for LBL5-15 samples are moved right slightly due to zero shift from instrument.

of between 100–400 nm on the surface of the γ-Al_2O_3 (Fig. 2). All samples displayed octahedral MOF crystallites and support with less-defined shape. However, the charging of the samples and the support cover of some MOF crystallites made it difficult to do quantitative analysis of the structure of the LBL5, LBL10 and LBL15 for comparison. By qualitative observation, the crystallite sizes increased as more cycles were applied to the structure. To get a better quantitative correlation of MOF crystallite size as related to number of application cycles, X-ray diffraction was used to determine crystallite sizes for the LBL*x* samples by using a Williamson Hall plot (Fig. S2). However, this also proved to be unhelpful due to the overlap of reflections from γ-Al_2O_3, weak reflection intensity, and presence of smaller domains within visible crystals. The γ-Al_2O_3 XRD profile has broad reflections at 2θ = 19.6, 31.9, 37.6, 39.4, and 45.8° (Fig. 2). There are many sharper HKUST-1 reflections present, with the three most prominent being at 2θ = 9.5, 11.6, and 13.7°. The broadness of the γ-Al_2O_3 reflections is attributed to the weak crystalline nature of the material. In contrast, the HKUST-1 is highly crystalline and has narrow reflections. As the number of cycles increased these reflections were more prominent, indicating that the amount of HKUST-1 on the surface increased with layer count, in agreement with analysis of the corresponding ICP-MS results (Table 1).

Thermal gravimetric analysis (TGA) of the LBL*x* samples were obtained to provide further evidence that the application cycles indeed increased the MOF thin film thickness on the γ-Al_2O_3 as well as to determine the optimal temperature for MOF decomposition for the active catalyst. Illustrated in Fig. 3 are the profile changes for the γ-Al_2O_3 support; all LBL*x* samples, and a bulk HKUST-1 sample with the % mass loss shown in Table 1. All samples have a modest decrease in mass from 30 °C to *ca.* 100 °C, which can be attributed to surface water adsorbed from the atmosphere. The next decrease in mass loss for all samples is centered between 230 °C and 430 °C with an additional slow decomposition after 430 °C. The sharp decomposition starting at 230 °C can be attributed to the decomposition of the trimesic acid ligands (the decomposition and removal

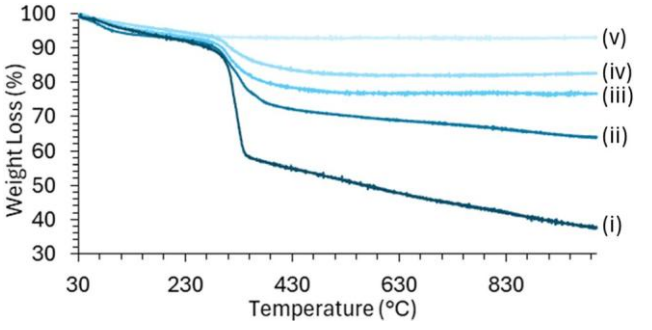

Fig. 3 Thermogravimetric analysis for the (i) bulk MOF sample, (ii) LBL15, (iii) LBL10, (iv) LBL5 and the (v) γ-Al_2O_3 support.

in the form of CO_2) for HKUST-1. The mass loss in the TGA for each sample increases with the number of cycles of HKUST-1 applied, indicating more MOF thin film is built up with the layered approach, which is consistent with the analysis of pXRD and N_2 adsorption measurements (Fig. 2 and Table 1).

3.2 Characterization of MOF precursor and derived copper nanoparticles

Using the TGA results of the templated samples, 350 °C was selected as the temperature to decompose the MOF thin films into the nanoparticle catalysts. Subsequently, samples were treated at 350 °C for 2 h under static air to remove the MOF matrix template. The materials were then heated again to 250 °C for 2 h under H_2 to reduce the MOF-derived CuO obtained *via* calcination to metallic Cu. To compare the catalytic performance of the LBL*x*D samples, a 10% Cu/γ-Al_2O_3 catalyst was prepared by a conventional sol-immobilization method. Typically, small and uniform nanoparticles can be prepared in solution by using a stabilizer such as poly(vinyl alcohol) (PVA) or polyvinylpyrrolidone (PVP) prior to deposition onto a support.[33,34] The catalyst surface area was 208 $m^2\ g^{-1}$ (Fig. S3) and the copper loading, along with TEM derived average particle size analysis are shown in Table 2. The targeted weight loading of Cu was 10 wt%, which is consistent with the ICP loading analysis of the resulting catalyst obtained by this method, and the Cu nanoparticles had a particle diameter of *ca.* 15 nm albeit with a narrower size distribution when compared to the LBL10D sample (*ca.* 11 nm) for example. The sol-immobilized catalyst was comparable to the LBL10D material in both Cu wt% and specific surface area.

The TGA mass loss% for the decomposed samples is shown in Table 2 with the thermograms of the samples in the SI (Fig. S4). No significant mass appears to be lost after decomposition (*ca.* 1% for all samples, Table 2). This negligible change in mass indicates successful removal of HKUST-1 template on γ-Al_2O_3. The samples were again analyzed using ICP-MS to determine the Cu content in the material (Table 2). Compared to the templated samples, the LBL*x*D samples increased in wt% due to the removal of the MOF template, with a larger increase for LBL15D which had more MOF on the powder support, from 12.4 to 20.7 wt%. The LBL5D sample had a minor concentration of MOF present, such that the remaining metal on the support (7 wt%) is comparable to the starting weight in the LBL5 sample.

BET surface area analysis (Table 2) showed an interesting trend with the samples. LBL5D and LBL10D samples show increased surface area compared to the support and undecomposed samples (Table 1 and Fig. S1). The particle sizes for both samples are likely small enough that they do not occlude the pores of the support. This allows the surface areas to increase to 273 and 292 $m^2\ g^{-1}$ for LBL5D and LBL10D respectively. Pore volume also increases to 1.66 and 1.94 $cm^3\ g^{-1}$ for each of these samples. However, the increased aggregation and particles sizes for LBL15D caused the pores of the γ-Al_2O_3 to be obstructed, which resulted in a substantial decrease in the surface area to 179 $m^2\ g^{-1}$. 10% Cu/γ-Al_2O_3 also appears to have decreased surface area (208 $m^2\ g^{-1}$) compared with the bare support. This indicates that the γ-Al_2O_3 pores are being blocked by the Cu particles, however, not to the extent present in the LBL15D sample.

Analysis of TEM images provided information about Cu particle size, distribution and aggregation. Fig. 4 shows the TEM images for the decomposed samples and the particle size distribution, where the particles appear as bright circular regions for STEM mode (a–c) and dark circles for dark-field mode (e) The average particle size increased with the increasing number of cycles as well as the broadening distribution of particle sizes. LBL5D resulted in the smallest particles, with a size distribution centered around 6–8 nm (7 ± 2 nm). Ten cycles of MOF application resulted in particle sizes centered around 9–13 nm for the LBL10D catalyst (11 ± 4 nm). Fifteen cycles resulted in a broader distribution compared to the other two samples with a distribution centered around 16–32 nm (28 ± 11 nm). This is due to larger sizes of the precursor MOF crystals, as larger crystals make aggregation of derived Cu particles more likely.

The step wise increase in Cu particle size was unexpected as the MOF template was hypothesized to hold the nanoparticles in place and restrict aggregation. However, the amount of MOF present indicates that agglomeration is still possible during the decomposition method. This result is currently being investigated further to determine how to minimize aggregation during decomposition of the template and ensure small particle sizes. The size of the nanoparticles through templating, 11 nm, is slightly smaller if not comparable to that for the sol immobilization method of preparation, 15 nm. The processing conditions were kept the same for the formation of the active copper nanoparticle catalysts. Therefore, LBL10D was chosen for analysis as a comparison of catalytic performance to the conventional catalyst because its properties were most similar.

Table 2 Characterization data for the Cu-based nanoparticle catalysts

Catalyst	Specific surface area ($m^2\ g^{-1}$)	Pore volume ($cm^3\ g^{-1}$)	ICP wt% Cu	TGA (wt% loss)	Mean nanoparticle diameter
LBL5D	273	1.66	6.9 ± 2.4	1.1	7 ± 2
LBL10D	292	1.94	10.4 ± 0.3	1.0	11 ± 4
LBL15D	179	1.51	20.7 ± 0.7	1.1	28 ± 11
10% Cu/γ-Al_2O_3	208	0.58	10.0	NA	15 ± 4

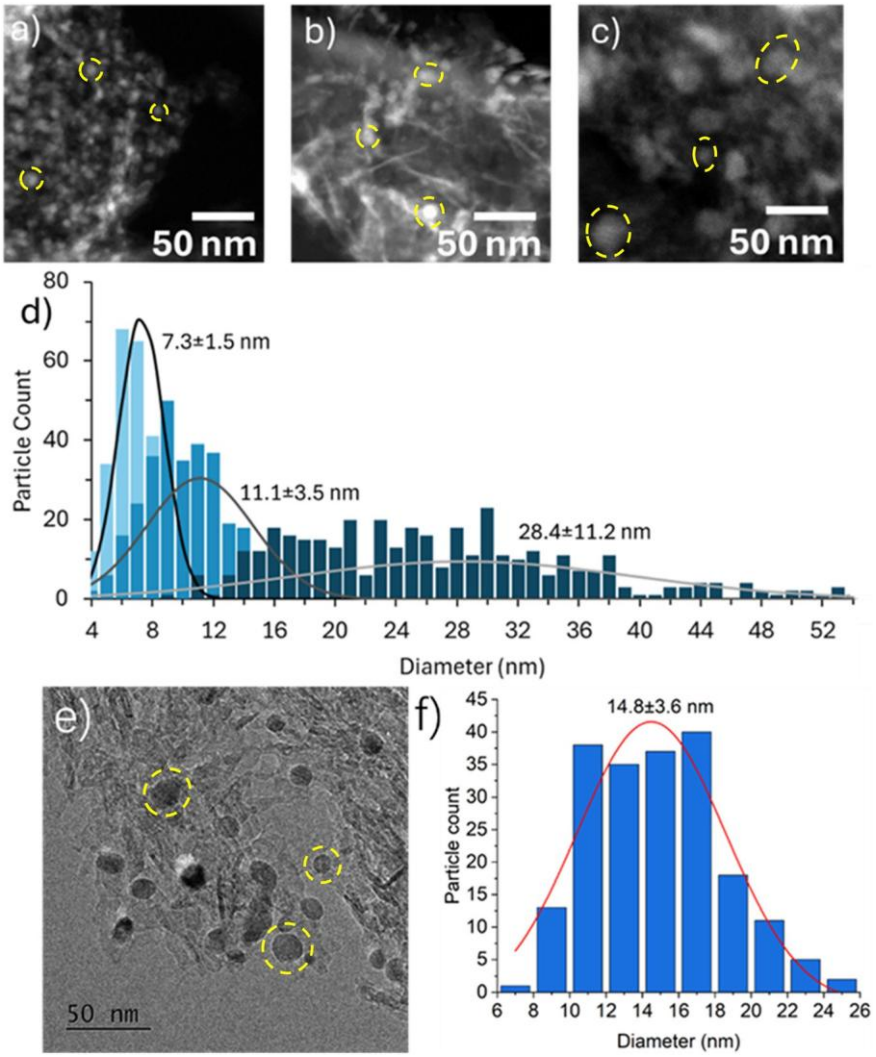

Fig. 4 Microscopy imaging for the MOF-derived nanoparticle samples a) LBL5D, b) LBL10D c) LBL15D, and e) 10% Cu/γ-Al_2O_3 with selected Cu nanoparticles marked by dashed circles, Cu particle size distribution analysis from TEM for d) each of the LBL-derived samples, and f) 10% Cu/γ-Al_2O_3. Full graph of LBLxD distribution (up to 77 nm) available in SI (Fig. S5).

The powder XRD for the catalysts, the conventional Cu catalyst and the LBL*x*D catalyst are shown in Fig. 5. The diffraction patterns indicate the presence of γ-Al_2O_3 and elemental copper in the samples, with Cu reflections at 2θ = 43.4 and 50.4°, and several surrounding γ-Al_2O_3 reflections at 2θ = 37.6, 39.4, 45.8, and 66.8°. The reflections corresponding to γ-Al_2O_3 are broader due to lower crystallinity of the support. The well-defined narrow reflections for LBL15D and 10% Cu/γ-Al_2O_3 samples indicate the presence of many larger Cu domains. For the samples LBL10D and LBL5D, the intensity of the reflections diminished considerably, indicating smaller, highly dispersive domains.

Results of the TPR analysis are shown in Fig. 6, where the 10% Cu/γ-Al_2O_3 and LBL10D catalysts have sharp reduction peaks at 229 °C and 232 °C respectively. Both samples show a further broad reduction between 600 and 800 °C. The lower temperature peak is attributed to the reduction of crystalline CuO to Cu.[35,36] Because the peak is at a relatively lower temperature this indicated the presence of smaller, well dispersed particles on the surface of both catalysts. The broad high temperature peak is attributed to amorphous CuO in the sample that is harder to reduce to its elemental components.[36] Due to the low intensity of this peak compared with the low temperature peak, there is much less amorphous CuO present than crystalline CuO. The amount of CuO present on both samples is comparable, as would be expected based on XPS and ICP results.

An additional characterization was obtained with the use of electron diffraction. As shown in Fig. 7, rings of spots were observed for the (111), (200), (220), and (311) planes of fcc Cu^0 at 4.785 1 nm^{-1}, 5.495 1 nm^{-1}, 7.752 1 nm^{-1}, and 8.475 1 nm^{-1} respectively.[37] This further confirms that Cu^0 is the major species present in the Cu particles. Because of the low concentration of copper which does not diffract at all necessary angles, spots are visible instead of clean rings. The variation in spot d-spacing for these rings is likely due to

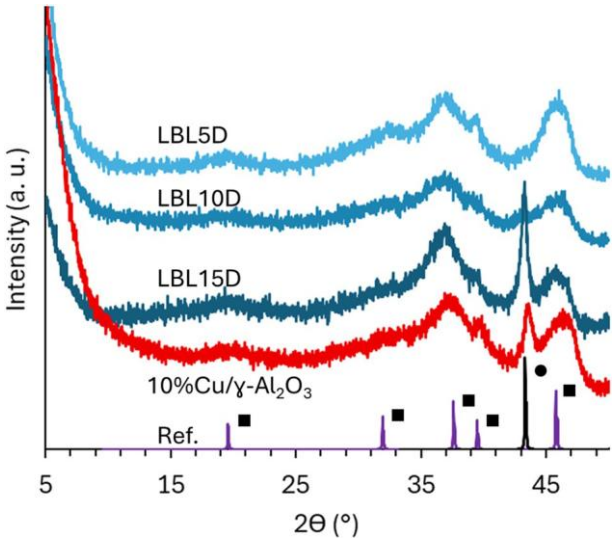

Fig. 5 Powder XRD for LBL5D, LBL10D, LBL15D, and 10% Cu/γ-Al_2O_3 samples. Along with computationally modeled references for (■) γ-Al_2O_3 (PDF 00-029-0063) and (●) Cu (PDF 01-085-1326).

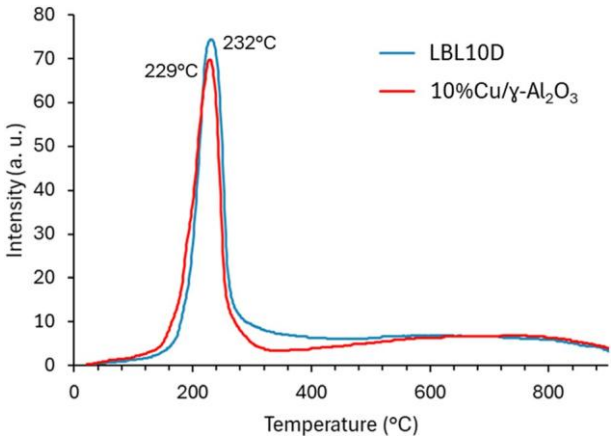

Fig. 6 TPR of the LBL10D (blue) and 10% Cu/γ-Al O (red) catalysts.

2 3

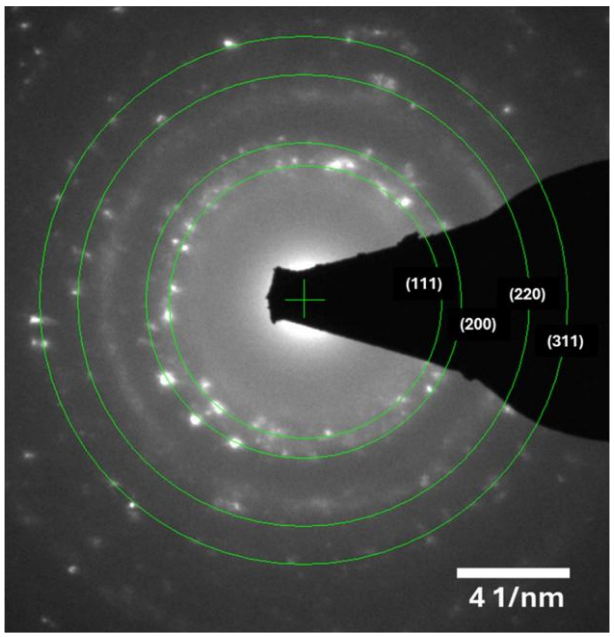

Fig. 7 Selected-area electron diffraction (SAED) for unused LBL10D.

lattice relaxation, which causes differences in the position/broadening of rings based on particle size.[38,39] Other bright spots present in the image can be attributed to the γ-Al_2O_3 support.[40] Combining this observation and the H_2-TPR and XRD results indicates that the active species is metallic Cu instead of oxidized Cu.

In addition to XRD, line scans and mapping were used to provide a clearer understanding of the elemental distribution in the catalyst. The line scans in Fig. 8 confirm that the Cu appears to be well confined to the particles. Throughout the spectra, the intensity of the Al and O peaks increase with the location of the line scan over the support. There are also small amounts of Al and O in the same locations as the Cu particle. This is likely the result of γ-Al_2O_3 present either above or below the nanoparticle. It can also be seen that the O peaks match well with the associated Al peaks, indicating that any spikes in oxygen are due to the γ-Al_2O_3 and not the copper particle. This again suggests that the Cu particles are in a reduced Cu state.

3.3 Activity and comparison of copper nanoparticle catalysts for CO_2 conversion

The catalytic CO_2 hydrogenation performance of the catalysts was evaluated at three different temperatures (230, 250, and 270 °C) under 20 bar after pre-reduction *in situ*, and the results are shown in Fig. 9. While long-term stability tests are important in CO_2 hydrogenation,[41] because the aim of these catalysts is to demonstrate a proof of concept in regard to the synthesis, we have not tested these catalysts beyond 90 hours.

In future iterations of this methodology, we will add Zn to the preparation,[42,43] and this will be more instructive to test on longer timescales due to the influence of the Zn on possible Cu restructuring[44,45] and the greater H_2O content of the reaction effluent[46–49] at such long times. The MOF-derived catalyst displayed similar if marginally better activity than the sol immobilization prepared catalyst. The equilibrium conversion of CO_2 at 230 °C, 250 °C, and 270 °C (20 bar) is 18%, 19.5%, and 21%, respectively.[49,50] The experimentally achieved CO_2 conversion is significantly lower than the equilibrium conversion at three different catalytic conditions, indicating both CO_2 hydrogenation to methanol and reverse water gas shift (RWGS) under the testing conditions are not limited by thermodynamic equilibrium (Fig. S6). Fig. 9 indicates the MOF-derived catalyst had a higher methanol selectivity over almost the same range of CO_2 conversions, of 3–14%, compared to the sol immobilized 10% Cu/γ-Al_2O_3 catalyst (18.6% *vs.* 16.3% at 230 °C, 12.0% *vs.* 10.4% at 250 °C, 8.2% *vs.* 7.3% at 270 °C). This increased performance is compared to similar Cu/Al_2O_3 catalysts, but still shows lower performance

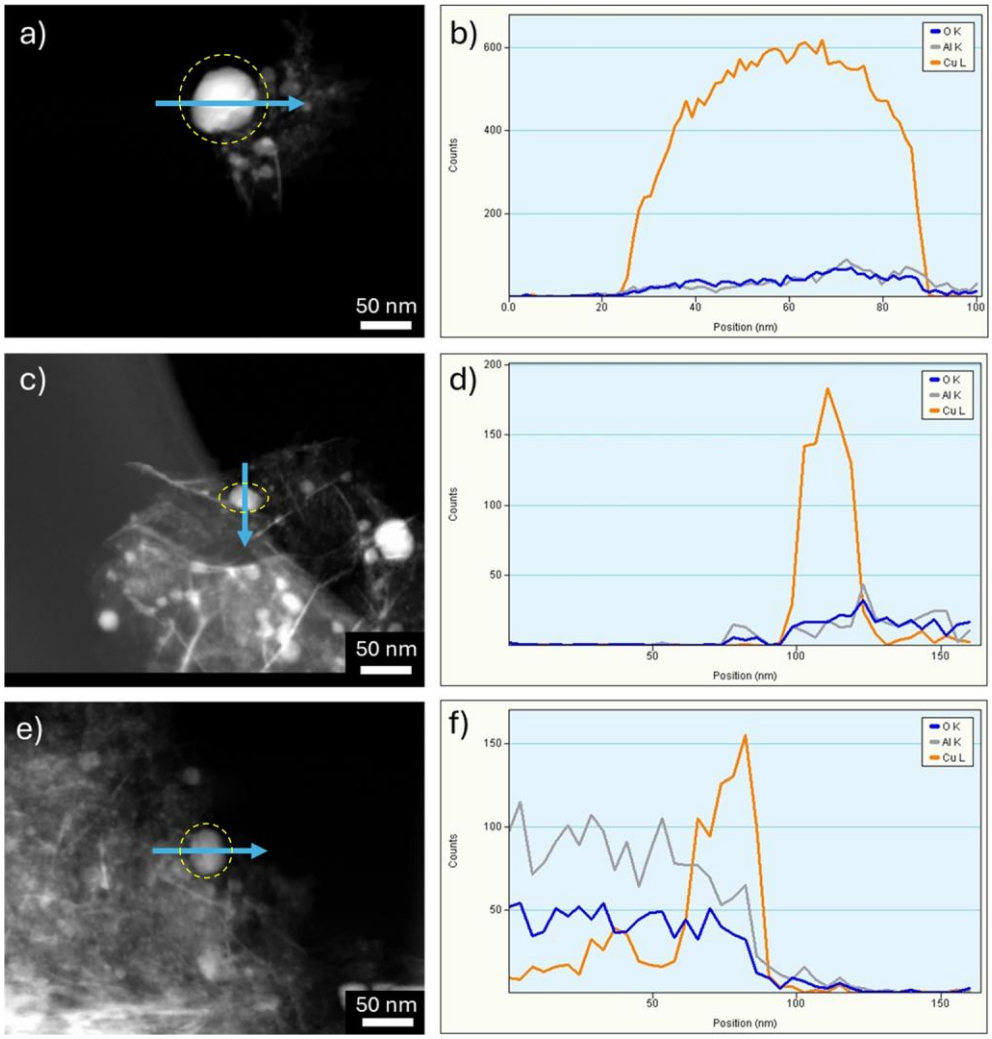

Fig. 8 Images of three different copper particles on the unused LBL10D catalyst with arrows depicting the direction of the scan and a dashed line outlining each particle imaged. (a, c and e) SEM images; (b, d and f) EDX line scans. SEM images correlate to the line scan directly opposite horizontally.

compared to catalysts containing other metal dopants. Potentially, this phenomenon can be ascribed to the previously reported relationship of Cu particle sizes on CO formation rate.[51] TEM images show that the Cu particles in the MOF-derived catalyst are significantly smaller than those in the conventional Cu catalyst prepared by sol-immobilization. A comparison of the catalyst particle density shows that the average number of Cu nanoparticles per nm^2 of catalyst for LBL10D is 0.00184 nanoparticles nm^{-2}, which is an order of magnitude greater than that for the 10% Cu/γ-Al_2O_3 catalyst (0.000136 nanoparticles per nm^2).[50] This result is highly aligned with the particle size difference verified by TEM and suggests more abundant interfacial sites between the copper and γ-Al_2O_3 for the LBL10D catalyst. The effect of Cu particle size has been shown to have a strong influence on CO_2-to-methanol selectivity whereas the TOF_{CO} was size-dependent and increased with Cu size increasing from 5 nm to 20 nm, while the TOF_{MeOH} was size-independent.[51] The observed particle size effect was attributed to the reduction in the number of active sites capable of promoting CO formation as particle size decreased. Furthermore, smaller Cu particle size typically leads to higher density of interfacial sites between the Cu and support. Previous studies found that a greater abundance of interfacial sites is favourable for increasing methanol selectivity due to its negligible effect on the CH_3OH formation rate but inhibition effect on the CO generation rate.[7] Hence, the enhanced methanol selectivity and productivity of the MOF-derived catalyst may be attributed to its smaller Cu particle size and optimized metal–support interface. As shown in Fig. 9 and S6, as the reaction temperature increased, CO_2 conversion and methanol productivity increased, while methanol selectivity decreased in favor of CO. Over both catalysts CO is the main product, followed by methanol and then DME, with negligible concentrations of methane produced. The product distribution is typical for the Cu/Al_2O_3 catalytic system for CO_2 hydrogenation to methanol.[52–54]

The catalytic activity of LBL10D and 10% Cu/γ-Al_2O_3 remained stable for *ca.* 36 h over each temperature, whereas the undecomposed LBL10 material displayed a changing

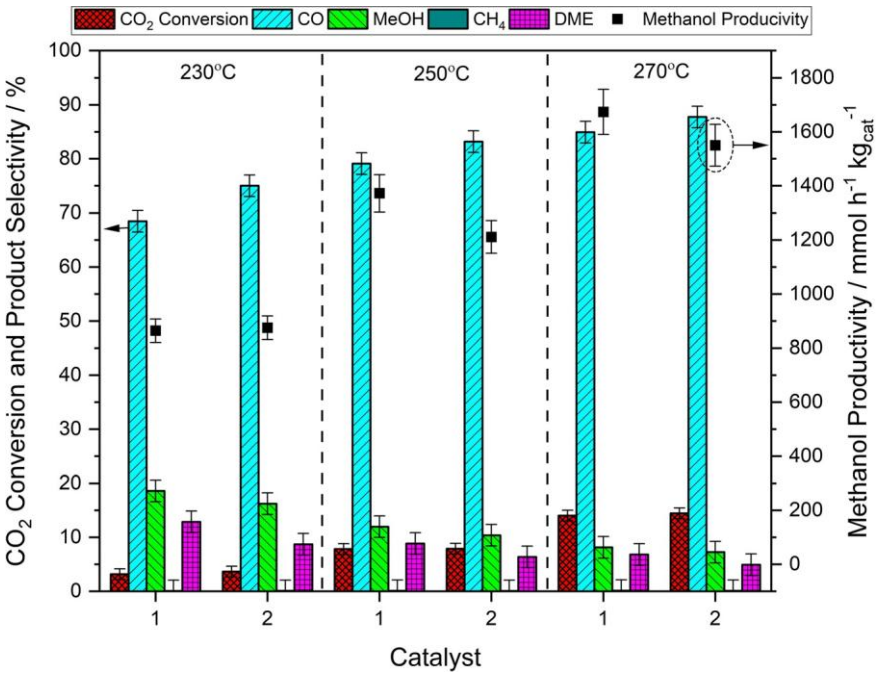

Fig. 9 Catalytic performance for CO_2 hydrogenation over LBL10D (catalyst 1) and 10% Cu/γ-Al_2O_3 (catalyst 2). Reaction conditions: 230-250-270 °C, 20 bar, 30 ml min^{-1}, $CO_2 : H_2 : Ar : N_2$ = 20 : 60 : 5 : 15, 0.1 g catalyst.

product distribution at 230 °C, which was not seen at the higher temperatures (Fig. S7). This difference in product distribution at this temperature is likely caused by the incomplete decomposition of the MOF precursor. Meanwhile, Fig. S6 showed that LBL10, the precursor of LBL10D, exhibited much lower activity than LBL10D, highlighting the crucial role of decomposition of the MOF in achieving enhanced performance.

The methanol productivity over LBL10D was calculated to be *ca.* 1700 mmol h^{-1} kg^{-1} at 270 °C and 20 bar which compares to previously reported values over Cu/H-600 (10 wt% Cu/Al_2O_3) of *ca.* 2500 mmol h^{-1} kg^{-1} at 280 °C and 30 bar (60 ml min^{-1}, CO_2 : H_2 = 1 : 3) when 0.5 g catalyst was used[28] and Cu/Al_2O_3 (15 wt% Cu) of *ca.* 2500 mmol h^{-1} kg^{-1} at 280 °C and 40 bar (40 ml min^{-1}, $CO_2 : H_2 : N_2$ = 3 : 9 : 1) when 0.4 g catalyst was used (Table S1).[36] Though the catalyst showed promise compared to similar Cu/Al_2O_3, the absence of ZnO hinders its final performance. The presence of ZnO, as found in the commercial Cu–ZnO–Al_2O_3 (CZA) catalyst promotes methanol selectivity and productivity, when ZnO is absent the RWGS pathway is favored. Accordingly, over CZA a methanol productivity of 4226 mmol h^{-1} kg^{-1} was achieved at 270 °C and 20 bar (30 ml min^{-1} $CO_2 : H_2 : Ar : N_2$ = 20 : 60 : 5 : 15) when 0.1 g catalyst was used. Although the Cu loading of CZA is higher at *ca.* 60 wt%, ZnO is considered a key component of the catalyst as this can adsorb CO_2 and provides interfacial active sites with Cu facilitating the formation of methanol.[42,55,56] Future work should include the addition of ZnO to improve methanol selectivity; however, this initial study serves as preliminary data highlighting the effective catalyst preparation using decomposed MOF structures.

As shown in Fig. 10, both fresh and used catalysts exhibit Cu^{2+} (as represented by purple peaks) and metallic Cu (red peaks). Given the catalysts are analyzed *ex situ*, and therefore exposed to moist air, we attribute the Cu^{2+} to $Cu(OH)_2$ which is also consistent with binding energy of the Cu^{2+} peak (934.7 eV) and the enhanced reduction under X-ray analysis.[57] The lower peak is centered at 932.6 eV and can be attributed to either metallic Cu or Cu^+ discernable only by use of the Auger parameter.[57,58] However, the instability to the Cu species to the X-ray analysis and the weaker Auger structure preclude a reliable analysis, even with fitting,[57] regardless of this, vectorial analysis (not shown)[59] of the Cu Auger reveals an Auger parameter of 1849.5 eV (±0.3 eV) a value typically consistent with Cu^+ species, or small metallic Cu clusters where the degree of electrostatic screening is reduced.[60] After reaction, part of the surface metallic Cu or Cu^+ species was oxidized to Cu^{2+}, which was likely caused by the existence of CO_2 and produced water under reaction conditions.[46] The XRD profile of LBL10D remained nearly unchanged after reaction, confirming its high stability, while 10% Cu/γ-Al_2O_3 was not as stable, and the Cu diffraction peaks of 10% Cu/γ-Al_2O_3 disappeared after the reaction, which may have resulted from water-assisted redispersion, atomic thermal diffusion of Cu,[44,45] and/or Cu oxidation which is somewhat validated by XPS. It's difficult to compare the performance of the LBL synthesized catalyst due to lack of references using similar catalysts (Cu wt%) and similar conditions (Table S1). The authors could only find one literature comparison with the same catalyst composition and reaction conditions.[61]

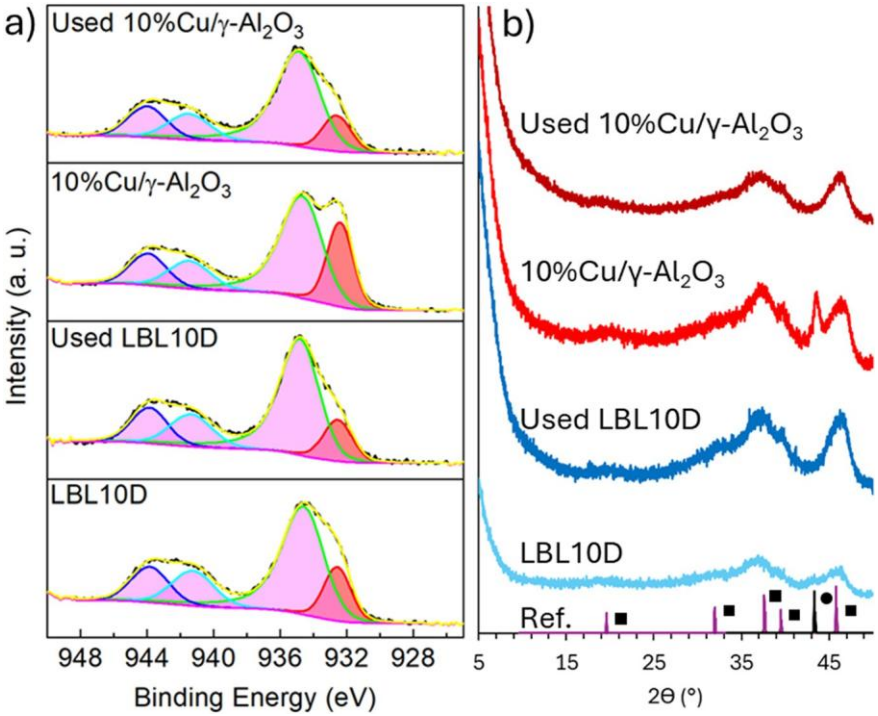

Fig. 10 a) XPS spectra of Cu $2p_{3/2}$ of LBL10D and 10% Cu/γ-Al_2O_3 before and after reaction. b) XRD patterns for LBL10D and 10% Cu/γ-Al_2O_3 before and after catalyst testing. Along with computationally modeled references for (■) γ-Al_2O_3 (PDF 00-029-0063) and (●) Cu (PDF 01-085-1326).

This catalyst performed similar or slightly better than the LBL catalysts. This provides a framework where the LBL10 catalyst performed marginally better than a catalyst synthesized *via* a solvothermal method and performed marginally worse than a catalyst synthesized *via* impregnation.

Post-reaction TEM images were obtained to determine if there was any Cu agglomeration during the reaction and are displayed in Fig. S8 for LBL10D and 10% Cu/γ-Al_2O_3. Though it is challenging to clearly observe Cu nanoparticles on the used catalysts using TEM, no agglomeration was seen and instead it appears that the nanoparticles have redispersed with diameters of around 3 nm for each of the two catalysts.

The decision to use 20 bar as the operating pressure for CO_2 hydrogenation which is consistent with lower energy requirements for a "green fuels" route is consistent with a variety of product outcomes. The mechanism for hydrogenation of CO_2 has multiple pathways by which it can proceed,[7,62] including the HCOO,[63,64] r-HCOO,[65] RWGS + CO-hydro,[63] and *trans*-COOH pathways.[66] The pathway is dependent on reaction conditions, metal oxidation state, and presence of secondary metal ions.[67–69] Our focus regarding mechanism will be on the pathways relevant to Cu supported on γ-Al_2O_3. As for metal/oxide catalysts including Cu/Al_2O_3, CO_2 is generally activated and bound at the metal/oxide interface, while the dissociation of molecular H_2 occur easily on the metal sites, followed by hydrogen spillover.[7,70] Based on the results of multiple studies the Cu/γ-Al_2O_3 catalyst likely proceeds through the formate (HCOO) pathway.[7,71,72] The formate pathway proceeds as follows: i) H* binds to CO_2 mediated by the copper surface, creating the HCOO molecule dioxymethylene; ii) it proceeds through a H* addition step to form formic acid (HCOOH); iii) another H* is added to form CH_2OOH*; iv) cleavage then occurs to form surface bound CH_2O and OH*; v) addition of another H* creates surface bound CH_3O, the second identifiable intermediate; vi) protonation then forms and releases methanol.[73] Giving the progression:

$$CO^*_2 \rightarrow HCOO^* \rightarrow HCOOH^* \rightarrow CH_2OOH^* \rightarrow CH_2O^* \rightarrow CH_3O^* \rightarrow CH_3OH(g)$$

CO coordinated on Cu desorbs while further hydrogenation of the O* located at the interface yields H_2O that desorbs as well. Reverse water gas shift (RWGS) reaction pathways involve CO_2 adsorbed at the interface of the Cu nanoparticle and Al_2O_3 which directly splits into CO* and O* *via* the direct C–O bond cleavage pathway.[7,51] For copper, the reaction proceeds through the dissociation pathway as confirmed by both DFT and *in situ* studies and shown in the overall reaction below:[74,75]

$$CO_2(g) + H_2(g) \rightarrow CO^*_2 + 2H^* \rightarrow CO^* + O^* + 2H^* \rightarrow CO^* + OH^* + H^* \rightarrow CO^* + H_2O^* \rightarrow CO(g) + H_2O(g)$$

Here, both CO_2 and H_2 adsorb to the support. Then the C–O and H–H bond are cleaved. Now instead of binding with the adsorbed CO_2 for the methanol route, one H* bonds with O* in succession to eventually form H_2O*. Finally, the CO(g) and H_2O(g) are produced.[75] This reaction is mildly endothermic

(42.1 KJ mol^{-1}) which indicates that the production of CO increases with temperature.

Notably, in comparison to γ-Al_2O_3, Cu has a higher affinity for H_2, and decreases the production of CO.[76] Furthermore, the active sites present on γ-Al_2O_3 stabilize the intermediates and support methanol formation.[72] This increase in selectivity at interfacial Cu sites is further supported by DFT studies where the synergistic effect between the metal and oxide in promoting CO_2 conversion to CH_3OH was observed in Cu/oxide catalysts, surpassing the activity of Cu catalysts without oxide supports.[70] However, we do see an increase in CO with increasing temperature under our conditions as shown in Fig. 9.[77] Interestingly, the Lewis acidity of the γ-Al_2O_3, has also shown increases to the production of CO and DME.[65] DFT studies have found that DME exhibits weaker adsorption on the catalyst surface compared with other intermediates and products, such as CH_3OH and H_2O.[7] Another key factor that may favor the RWGS pathway is the crystallinity of copper and the interaction with the γ-Al_2O_3 support. Previous studies have found that less crystalline Cu^0 helps promote the conversion of CO_2.[78] Other studies have shown that increasing the distance between Cu^0 particles on the support may cause a decrease in the selectivity toward CO by preventing hydrogen spillover.[49,79] However, this appears to contradict our results as the LBL10D has lower Cu^0 crystallinity (Fig. 5) and a smaller distance between Cu particles (Fig. 4). However, without further *in situ*/operando spectroscopies or system-specific DFT it is impossible to assign the product selectivity and outcomes to the methanol or the RWGS pathway as they share common intermediates, especially at conservative pressures. The studies referenced here are to provide mechanistic plausibility, but we cannot definitely claim and only instead frame our conclusions as consistent with these models. The difference in particle size appears to be the largest contributor to the lower CO selectivity for the LBL10D product. Our mechanistic interpretation is intentionally bounded by our measurements; definitive assignments would require *in situ*/operando characterization or system specific DFT, which we identify as future work.

4. Conclusions

A γ-Al_2O_3 supported copper nanoparticle catalyst was successfully synthesized using layer-by-layer MOF growth then decomposition. The catalyst had variable wt% of Cu (6.9 to 20.7) and particle size (7 ± 2 to 28 ± 11 nm) depending on layers of growth. Though originally hypothesized to prevent aggregation, larger MOF quantities still resulted in larger particle sizes. The sample with ten layers of growth, LBL10D, was chosen for further testing. When compared to a traditionally synthesized supported copper catalyst, the LBL10D catalyst had similar CO_2 conversion, but had increased methanol selectivity and productivity at all temperatures. It is likely that a RWGS reaction is also occurring especially due to the absence of ZnO and other secondary metals as well as the conservative 20 bar pressure in operating conditions. The increase in outcomes for the LBL10D catalyst is likely due to the smaller particle sizes (15 nm for traditional *vs.* 11 nm for MOF derived). Characterization of the catalysts through TPR and XPS showed that both catalysts had similar chemical properties, specifically pertaining to the quantity of copper in Cu^{2+} and Cu^0 oxidation states. Post-catalysis characterization showed formation of Cu^{2+} which is consistent with water production during the reaction, and TEM results showed minimal particle aggregation post-reaction. The catalyst was tested twice at each temperature which resulted in similar data indicating reproducibility of the method. To expand on this work, future studies would explore the use of additives such as Mg or ZnO to help improve catalyst performance.

Author contributions

Adele T Chalmers synthesized and analyzed samples, wrote and revised paper. Zonggao Hu synthesized and analyzed samples, analyzed catalytic performance, wrote and revised paper. Nicholas F. Dummer analyzed catalytic performance of both catalysts, wrote and revised paper, and helped initially conceptualize project and aided in project supervision. Kieran J. Aggett contributed to analysis of catalytic performance and writing. David J. Morgan assisted with analysis of samples and writing/revisions of results for XPS data. Michael Bowker and Graham Hutchings helped initially conceptualize project. Kara Stowers initially conceptualized project, wrote and revised paper, helped analyze LBL*x*/LBL*x*D samples and aided in full project supervision.

Conflicts of interest

The authors declare no conflict of interest.

Data availability

The data supporting this article have been included as part of the supplementary information (SI). Supplementary information: additional analyses and experimental methods are available including; parameters for the bulk HKUST-1 synthesis, a table comparing the catalyst with more literature values, N_2 isotherms, Williamson-hall plots (LBL*x*), additional TGA curves, full particle size distribution of LBL*x*D samples, graphs of methanol/CO selectivity as a function of CO_2 conversion, catalytic performance for individual samples, and post-reaction TEM images. See DOI: https://doi.org/10.1039/d5cy01235j.

Other additional information is available upon request.

Acknowledgements

The authors would like to acknowledge the financial support from the EPRSC grant "Parallel-screening equipment for advanced catalyst testing and process intensification" (EP/P001467/1) as well as National Science Foundation funding

under grant 2349338. The authors would like to thank the Max Planck Society and Cardiff University for the financial support to create the Max Planck-Cardiff FUNCAT Centre. We would also like to acknowledge Integrated Lab Solutions (ILS) for the design and manufacture of the high throughput reactor used for catalyst testing, alongside their continued support and technical expertise.

References

1 S.-T. Bai, G. De Smet, Y. Liao, R. Sun, C. Zhou, M. Beller, B. U. Maes and B. F. Sels, *Chem. Soc. Rev.*, 2021, 50, 4259–4298.
2 L. Fan, Z. Tu and S. H. Chan, *Energy Rep.*, 2021, 7, 8421–8446.
3 G. Pacchioni, *ACS Catal.*, 2024, 14, 2730–2745.
4 T. Kamsuwan, A. Guntida, P. Praserthdam and B. Jongsomjit, *ACS Omega*, 2022, 7, 25783–25797.
5 T. Witoon, S. Bumrungsalee, M. Chareonpanich and J. Limtrakul, *Energy Convers. Manage.*, 2015, 103, 886–894.
6 P. Tahay, Y. Khani, M. Jabari, F. Bahadoran, N. Safari and A. Zamanian, *Int. J. Hydrogen Energy*, 2020, 45, 9484–9495.
7 E. Lam, J. J. Corral-Pérez, K. Larmier, G. Noh, P. Wolf, A. Comas-Vives, A. Urakawa and C. Copéret, *Angew. Chem., Int. Ed.*, 2019, 58, 13989–13996.
8 S. Lamouri, M. Hamidouche, N. Bouaouadja, H. Belhouchet, V. Garnier, G. Fantozzi and J. F. Trelkat, *Bol. Soc. Esp. Ceram. Vidrio*, 2017, 56, 47–54.
9 R. Prins, *J. Catal.*, 2020, 392, 336–346.
10 M. Trueba and S. P. Trasatti, *Eur. J. Inorg. Chem.*, 2005, 2005, 3393–3403.
11 W. Zhang, K. Zhu, W. Ren, H. He, H. Liang, Y. Zhai and W. Li, *Adv. Mater. Interfaces*, 2022, 9, 2101528.
12 A. Vinukonda, N. Bolledla, R. K. Jadi, R. Chinthala and V. R. Devadasu, *Next Nanotechnology*, 2025, 8, 100169.
13 X. Shi, Y. Shan, M. Du and H. Pang, *Coord. Chem. Rev.*, 2021, 444, 214060.
14 H.-C. Zhou, J. R. Long and O. M. Yaghi, *Chem. Rev.*, 2012, 112, 673–674.
15 H. C. Anderson, M. Rawlins, A. A. Prue, L. M. Sanders, F. Rivera and K. J. Stowers, *J. Mater. Chem. A*, 2022, 10, 17680–17690.
16 X. Guo, S. Geng, M. Zhuo, Y. Chen, M. J. Zaworotko, P. Cheng and Z. Zhang, *Coord. Chem. Rev.*, 2019, 391, 44–68.
17 A. H. N. Sorenson, Y. Wu, E. K. Orcutt, R. V. Kent, H. C. Anderson, A. J. Matzger and K. J. Stowers, *J. Mater. Chem. A*, 2020, 8, 15066–15073.
18 V. Chernikova, O. Shekhah and M. Eddaoudi, *ACS Appl. Mater. Interfaces*, 2016, 8, 20459–20464.
19 C. H. Bartholomew, B. F. Woodfield, B. Huang, R. E. Olsen and L. Astle, *US Pat.*, US9334173B2, 2016.
20 B. Huang, C. H. Bartholomew, S. J. Smith and B. F. Woodfield, *Microporous Mesoporous Mater.*, 2013, 165, 70–78.
21 B. Huang, C. H. Bartholomew and B. F. Woodfield, *Microporous Mesoporous Mater.*, 2014, 183, 37–47.
22 S. J. Smith, B. Huang, S. Liu, Q. Liu, R. E. Olsen, J. Boerio-Goates and B. F. Woodfield, *Nanoscale*, 2015, 7, 144–156.
23 N. Fairley, V. Fernandez, M. Richard-Plouet, C. Guillot-Deudon, J. Walton, E. Smith, D. Flahaut, M. Greiner, M. Biesinger and S. Tougaard, *Appl. Surf. Sci. Adv.*, 2021, 5, 100112.
24 D. J. Morgan, *Surf. Interface Anal.*, 2025, 57, 28–35.
25 Z. Wang and C. Wöll, *Adv. Mater. Technol.*, 2019, 4, 1800413.
26 M. E. Silvestre, M. Franzreb, P. G. Weidler, O. Shekhah and C. Wöll, *Adv. Funct. Mater.*, 2013, 23, 1210–1213.
27 X. Ma, S. Peng, W. Li, H. Liu and Y. Chen, *CrystEngComm*, 2018, 20, 407–411.
28 N. Kanjanasoontorn, T. Permsirivanich, T. Numpilai, T. Witoon, N. Chanlek, M. Niamlaem, C. Warakulwit and J. Limtrakul, *Catal. Lett.*, 2016, 146, 1943–1955.
29 J. Čejka, *Appl. Catal., A*, 2003, 254, 327–338.
30 N. Suzuki and Y. Yamauchi, *J. Sol-Gel Sci. Technol.*, 2010, 53, 428–433.
31 Y. Chen, X. Mu, E. Lester and T. Wu, *Prog. Nat. Sci.: Mater. Int.*, 2018, 28, 584–589.
32 J. S. Choi, J. Bae, E. J. Lee and N. C. Jeong, *Inorg. Chem.*, 2018, 57, 5225–5231.
33 X. Huang, O. Akdim, M. Douthwaite, K. Wang, L. Zhao, R. J. Lewis, S. Pattisson, I. T. Daniel, P. J. Miedziak and G. Shaw, *Nature*, 2022, 603, 271–275.
34 A. Villa, D. Wang, G. M. Veith, F. Vindigni and L. Prati, *Catal. Sci. Technol.*, 2013, 3, 3036–3041.
35 P. Ling, D. Li and X. Wang, *J. Mol. Catal. A: Chem.*, 2012, 357, 112–116.
36 S.-c. Zhang and Y. Bin, *Trans. Nonferrous Met. Soc. China*, 2011, 21, 2644–2648.
37 G. Cheng and A. Hight Walker, *Anal. Bioanal. Chem.*, 2010, 396, 1057–1069.
38 F. Zhang, S.-W. Chan, J. E. Spanier, E. Apak, Q. Jin, R. D. Robinson and I. P. Herman, *Appl. Phys. Lett.*, 2002, 80, 127–129.
39 Z. Zhu, T. Andelman, M. Yin, T.-L. Chen, S. N. Ehrlich, S. P. O'Brien and R. M. Osgood Jr, *J. Mater. Res.*, 2005, 20, 1033–1041.
40 H. O. Ayoola, S. D. House, C. S. Bonifacio, K. Kisslinger, W. A. Saidi and J. C. Yang, *Acta Mater.*, 2020, 182, 257–266.
41 T. Lunkenbein, F. Girgsdies, T. Kandemir, N. Thomas, M. Behrens, R. Schlögl and E. Frei, *Angew. Chem., Int. Ed.*, 2016, 55, 12708–12712.
42 S. Kattel, P. J. Ramírez, J. G. Chen, J. A. Rodriguez and P. Liu, *Science*, 2017, 355, 1296–1299.
43 D. Kordus, S. Widrinna, J. Timoshenko, M. Lopez Luna, C. Rettenmaier, S. W. Chee, E. Ortega, O. Karslioglu, S. Kühl and B. Roldan Cuenya, *J. Am. Chem. Soc.*, 2024, 146, 8677–8687.
44 Y. Fan, R. Li, B. Wang, X. Feng, X. Du, C. Liu, F. Wang, C. Liu, C. Dong and Y. Ning, *Nat. Commun.*, 2024, 15, 3046.
45 D. Yao, Y. Wang, Y. Li, A. Li, Z. Zhen, J. Lv, F. Sun, R. Yang, J. Luo and Z. Jiang, *Nat. Commun.*, 2023, 14, 1123.
46 B. Liang, J. Ma, X. Su, C. Yang, H. Duan, H. Zhou, S. Deng, L. Li and Y. Huang, *Ind. Eng. Chem. Res.*, 2019, 58, 9030–9037.
47 A. e. Prašnikar, A. Pavlišič, F. Ruiz-Zepeda, J. Kovač and B. Likozar, *Ind. Eng. Chem. Res.*, 2019, 58, 13021–13029.

48 J. Wu, M. Saito, M. Takeuchi and T. Watanabe, *Appl. Catal., A*, 2001, 218, 235–240.
49 J. Zhong, X. Yang, Z. Wu, B. Liang, Y. Huang and T. Zhang, *Chem. Soc. Rev.*, 2020, 49, 1385–1413.
50 R. Beerthuis, J. W. de Rijk, J. M. Deeley, G. J. Sunley, K. P. de Jong and P. E. de Jongh, *J. Catal.*, 2020, 388, 30–37.
51 L. Barberis, A. H. Hakimioun, P. N. Plessow, N. L. Visser, J. A. Stewart, B. D. Vandegehuchte, F. Studt and P. E. de Jongh, *Nanoscale*, 2022, 14, 13551–13560.
52 S. Li, Y. Wang, B. Yang and L. Guo, *Appl. Catal., A*, 2019, 571, 51–60.
53 K. K. Bando, K. Sayama, H. Kusama, K. Okabe and H. Arakawa, *Appl. Catal., A*, 1997, 165, 391–409.
54 N. Kanjanasoontorn, T. Permsirivanich, T. Numpilai, T. Witoon, N. Chanlek, M. Niamlaem, C. Warakulwit and J. Limtrakul, *Catal. Lett.*, 2016, 146, 1943–1955.
55 A. Beck, M. A. Newton, L. G. van de Water and J. A. van Bokhoven, *Chem. Rev.*, 2024, 124, 4543–4678.
56 Y. Shu, Z. Zhang, P. Wang, Z. Ma, S. Bi, M. Shi and P. Zhang, *Chem. Eng. J.*, 2024, 499, 155826.
57 M. C. Biesinger, *Surf. Interface Anal.*, 2017, 49, 1325–1334.
58 S. Poulston, P. Parlett, P. Stone and M. Bowker, Surface and Interface Analysis: An International Journal devoted to the development and application of techniques for the analysis of surfaces, interfaces and thin films, 1996, vol. 24, pp. 811–820.
59 V. Fernandez, D. Kiani, N. Fairley, F.-X. Felpin and J. Baltrusaitis, *Appl. Surf. Sci.*, 2020, 505, 143841.
60 G. Moretti, A. Palma, E. Paparazzo and M. Satta, *Surf. Sci.*, 2016, 646, 298–305.
61 H. Ren, C.-H. Xu, H.-Y. Zhao, Y.-X. Wang, J. Liu and J.-Y. Liu, *J. Ind. Eng. Chem.*, 2015, 28, 261–267.
62 M. Bersani, K. Gupta, A. K. Mishra, R. Lanza, S. R. Taylor, H.-U. Islam, N. Hollingsworth, C. Hardacre, N. H. De Leeuw and J. A. Darr, *ACS Catal.*, 2016, 6, 5823–5833.
63 L. Grabow and M. Mavrikakis, *ACS Catal.*, 2011, 1, 365–384.
64 E. L. Kunkes, F. Studt, F. Abild-Pedersen, R. Schlögl and M. Behrens, *J. Catal.*, 2015, 328, 43–48.
65 Y. Yang, C. A. Mims, R. S. Disselkamp, J.-H. Kwak, C. H. Peden and C. Campbell, *J. Phys. Chem. C*, 2010, 114, 17205–17211.
66 Y.-F. Zhao, Y. Yang, C. Mims, C. H. Peden, J. Li and D. Mei, *J. Catal.*, 2011, 281, 199–211.
67 L. Gao and C. Au, *J. Catal.*, 2000, 189, 1–15.
68 X. Nie, X. Jiang, H. Wang, W. Luo, M. J. Janik, Y. Chen, X. Guo and C. Song, *ACS Catal.*, 2018, 8, 4873–4892.
69 J. Zhang, X. Sun, C. Wu, W. Hang, X. Hu, D. Qiao and B. Yan, *J. Energy Chem.*, 2023, 77, 45–53.
70 S. Kattel, P. Liu and J. G. Chen, *J. Am. Chem. Soc.*, 2017, 139, 9739–9754.
71 S. Sajnani, M. A. Memon, S. A. Memon, A. Kumar, D. Mehvish, S. Ameen, W. Zhou and Y. Liu, *Processes*, 2025, 13, 314.
72 X. Song, C. Yang, X. Li, Z. Wang, C. Pei, Z.-J. Zhao and J. Gong, *ACS Catal.*, 2022, 12, 14162–14172.
73 P. Liu, Y. Yang, J. Evans, J. Rodriguez and M. White, *Phys. Chem. Chem. Phys.*, 2010, 12, 9909–9917.
74 L. Dietz, S. Piccinin and M. Maestri, *J. Phys. Chem. C*, 2015, 119, 4959–4966.
75 X. Yao, Z. Wei, J. Mei, X. Guo and X. Tian, *RSC Adv.*, 2025, 15, 460–466.
76 H. Liang, G. Zhang, Z. Li, Y. Zhang and P. Fu, *Fuel Process. Technol.*, 2023, 252, 107995.
77 Y. Choi, G. D. Sim, U. Jung, Y. Park, M. H. Youn, D. H. Chun, G. B. Rhim, K. Y. Kim and K. Y. Koo, *Chem. Eng. J.*, 2024, 492, 152283.
78 X. Ai, H. Xie, S. Chen, G. Zhang, B. Xu and G. Zhou, *Int. J. Hydrogen Energy*, 2022, 47, 14884–14895.
79 X. Cui, S. Chen, H. Yang, Y. Liu, H. Wang, H. Zhang, Y. Xue, G. Wang, Y. Niu and T. Deng, *Appl. Catal., B*, 2021, 298, 120590.